11-2011

An Ultrasonically Powered Implantable Micro-Oxygen Generator (IMOG)

Teimour Maleki
Purdue University, tmalekij@purdue.edu

Ning Cao
Purdue University, ncao@purdue.edu

Seung Hyun Song
Purdue University, song80@purdue.edu

Chinghai Kao

Song-Chu Ko
Purdue University

See next page for additional authors

Maleki, Teimour; Cao, Ning; Song, Seung Hyun; Kao, Chinghai; Ko, Song-Chu; and Ziaie, Babak, "An Ultrasonically Powered Implantable Micro-Oxygen Generator (IMOG)" (2011). *Birck and NCN Publications.* Paper 841.
http://dx.doi.org/10.1109/TBME.2011.2163634

An Ultrasonically Powered Implantable Micro-Oxygen Generator (IMOG)

Teimour Maleki*, *Member, IEEE*, Ning Cao, Seung Hyun Song, Chinghai Kao, Song-Chu "Arthur" Ko, and Babak Ziaie, *Senior Member, IEEE*

***Abstract*—In this paper, we present an ultrasonically powered implantable micro-oxygen generator (IMOG) that is capable of *in situ* tumor oxygenation through water electrolysis. Such active mode of oxygen generation is not affected by increased interstitial pressure or abnormal blood vessels that typically limit the systemic delivery of oxygen to hypoxic regions of solid tumors. Wireless ultrasonic powering (2.15 MHz) was employed to increase the penetration depth and eliminate the directional sensitivity associated with magnetic methods. In addition, ultrasonic powering allowed for further reduction in the total size of the implant by eliminating the need for a large area inductor. IMOG has an overall dimension of 1.2 mm $\times$ 1.3 mm $\times$ 8 mm, small enough to be implanted using a hypodermic needle or a trocar. *In vitro and ex vivo* experiments showed that IMOG is capable of generating more than 150 μA which, in turn, can create 0.525 μL/min of oxygen through electrolytic disassociation. *In vivo* experiments in a well-known hypoxic pancreatic tumor models (1 cm^3 in size) also verified adequate *in situ* tumor oxygenation in less than 10 min.**

***Index Terms*—Hypoxia, radiation treatment, tumor oxygenation, ultrasonic powering, water electrolysis.**

I. Introduction

RADIATION therapy along with surgery and chemotherapy is one of the three pillars of modern cancer treatment [1]. In radiation therapy, cancer cells are destroyed using high-energy photons (4–25 MeV) generated with a linear accelerator and directed onto the tumor [2]. Tumor cell death results mainly from direct and indirect DNA damage through ionizing radiation induced radiolysis of water [3].

In addition to accurate spatial delivery of precise radiation dosage, the efficacy of radiation therapy depends on the concentration of oxygen in solid tumors. This is in light of the fact that presence of oxygen enables the creation of free radical species with greater stability and longer lifetimes that are critical for permanent damage to the DNA [4], [5]. Many solid malignancies contain a central hypoxic region (areas with an oxygen partial pressure of $pO_2 \leq 2.5$ mmHg) that is particularly resistant to radiation therapy (when pO_2 drops to less than 3–4 mmHg, radio sensitivity reduces to less than half of a well-oxygenated tissue). This hypoxia is a result of several factors; the most important of which is the imbalance between supply and consumption of oxygen due to abnormal perfusion in tumor microcirculation [6]–[8].

Oxygenation of tumors prior to radiation therapy as a method for enhancing the efficacy of treatment has been investigated for many years. Two methods to achieve this goal have been reported. One forces patients to breathe an air mixture with higher oxygen content and the second one is hyperbaric oxygen therapy (HBOT). As expected, tumor oxygen levels can be elevated by increasing the arterial oxygen supply to the tissue. Higher tumor oxygenation can be accomplished by asking patients to breathe high-oxygen content gases such as Carbogen (95% O_2 and 5% CO_2) [9], [10]. In spite of reasonable clinical outcomes, due to severe acute toxicity and significant dropout rate, this approach is not commonly used in clinical settings in the U.S. HBOT delivers 100% (or nearly 100%) oxygen at pressures greater than 1 atm [11]. However, due to safety issues stemming from high flammability of pure oxygen, systemic side effects (e.g., high fever, asthma, and seizures), and negative indication for patients with congestive heart failure, HBOT has not been widely adopted.

The two methods described earlier rely on systemic delivery of oxygen through respiratory system which in addition to the aforementioned problems lack adequate control over exact delivery of oxygen to hypoxic regions of tumors. In this paper, we report on an implantable microdevice that is capable of *in situ* tumor oxygenation through simple water electrolysis. Such active and local mode of oxygen generation is not affected by increased interstitial pressure or abnormal tumor microcirculation that typically limits the delivery of oxygen to hypoxic regions. In addition, implantation of a miniature oxygen generator provides a high degree of spatial and temporal controls that are not achievable though previously attempted systemic methods.

II. Microdevice Operation and Design

Fig. 1(a) shows a schematic of the implantable micro-oxygen generator (IMOG) located inside a pancreatic tumor and powered from outside with an ultrasonic transducer. Once energized, the device uses water present in the tissue to perform *in situ* electrolysis and generate oxygen. Fig. 1(b) shows a detailed

Manuscript received February 7, 2011; revised July 2, 2011; accepted July 15, 2011. Date of publication August 4, 2011; date of current version October 19, 2011. This work was supported by Alfred Mann Institute at Purdue. *Asterisk indicates corresponding author.*

*T. Maleki is with the Birck Nanotechnology Center, Purdue University, West Lafayette, IN 47906 USA (e-mail: tmalekij@purdue.edu).

N. Cao is with the Medical Physics Program, School of Health Sciences, Purdue University, West Lafayette, IN 47906 USA (e-mail: ncao@indiana.edu).

S. H. Song and B. Ziaie are with the School of Electrical and Computer Engineering, Purdue University, West Lafayette, IN 47906 USA (e-mail: song80@purdue.edu; bziaie@purdue.edu).

C. Kao is with the Department of Urology, Indiana University School of Medicine, Indianapolis, IN 46202 USA (e-mail: chkao@iupui.edu).

S.-C. A. Ko is with the Indiana University School of Medicine, Indianapolis, IN 46202 USA (e-mail: sko@iuhealth.org).

Color versions of one or more of the figures in this paper are available online at http://ieeexplore.ieee.org.

Digital Object Identifier 10.1109/TBME.2011.2163634

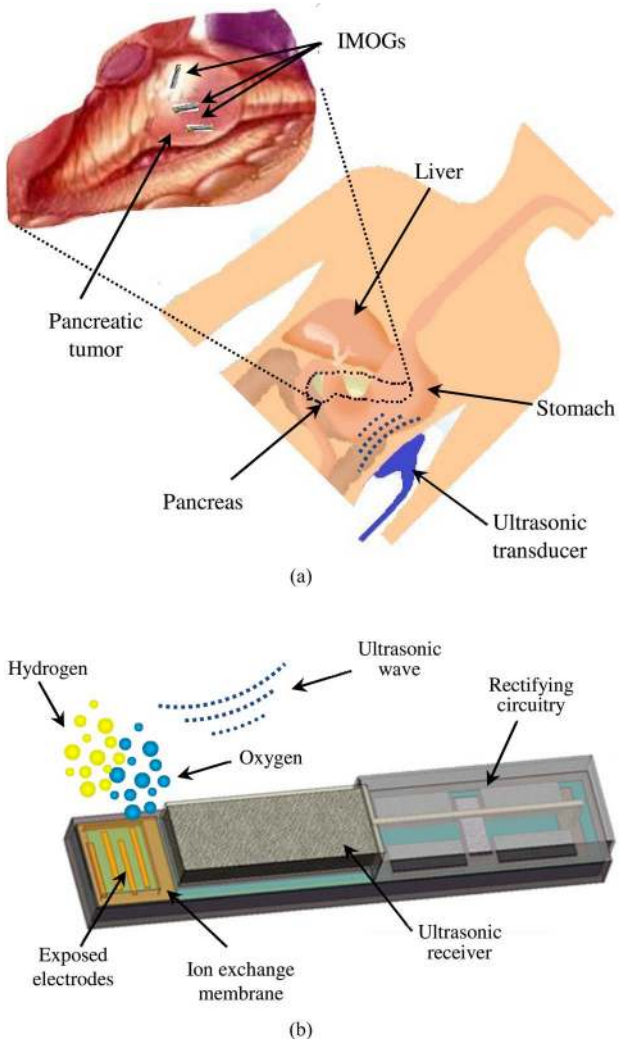

Fig. 1. (a) IMOG implanted in a pancreatic tumor for *in situ* oxygenation. (b) Detailed schematic of the IMOG showing various components such as ultrasonic receiver, rectifier circuitry, electrodes, and ion exchange membrane.

schematic of the IMOG illustrating various components including: 1) ultrasonic receiver; 2) rectifying circuitry; 3) electrodes; and 4) ion exchange membrane.

Using an on-board rectifying circuitry, IMOG converts ultrasonic power to a dc voltage that is then applied to a pair of platinum electrodes, generating oxygen through water electrolysis (the generated hydrogen is inert and is eventually eliminated through lungs) [12]. The size of the IMOG is 1.2 mm $\times$ 1.3 mm $\times$ 8 mm, making it suitable for easy insertion using a hypodermic biopsy needle. The small size also allows several microdevices to be implanted, if required.

A. Oxygen Generation

The amount of oxygen required to bring a hypoxic tumor to normal oxygen levels is a primary design concern. Interstitial medium typically occupies one-sixth of the tumor volume. For a tumor with total volume of 3 cm^3, the corresponding interstitial volume can be approximated to be $\sim$0.5 cm^3. The total required oxygen to achieve a normal oxygen partial pressure of 50 mmHg can be calculated by considering the phase equilibrium between $(O_2)_g$ and $(O_2)_{aq}$ given by [13]

$$C_{aq} = \phi \times k \times pO_2 \tag{1}$$

Where C_{aq} is oxygen solubility (*g/L*), pO_2 is oxygen partial pressure (in atm), k is the temperature dependent equilibrium constant (mol$(O_2)_{aq}$/kg H_2O/atm), and ϕ represent the effects of dissolved ions on the oxygen solubility which is given by

$$\phi = (1 + \kappa(C_I)^y)^{-h} \tag{2}$$

where C_I is the molal concentration of solute; κ, y, and h are ion specific constants that are obtained experimentally. Considering the ionic concentration ranges in human body, ϕ was selected to be 0.9. At body temperature (37 °C), the equilibrium constant k is 0.00108. Using these numbers, the desired target oxygen level can be calculated to be 6.395 $\times$ 10^{-5} (in mol/kg) which means that in 0.5 cm^3 (0.5 g) of interstitial water 3.197 $\times$ 10^{-8} mol of oxygen has to be generated to fully oxygenate the tumor. Creation of one oxygen molecule by decomposition of water requires four electrons; hence, to create 3.197 $\times$ 10^{-8} mol of oxygen, IMOG needs to provide 7.701 $\times$ 10^{16} electrons or 12.32 mC of charge. To achieve this level in 10 min activation (i.e., oxygen generation) prior to a radiation therapy session, IMOG should be at able to supply 20.5 μA of current. For larger tumor sizes, several IMOGs could be implanted to cover the entire malignant volume for adequate oxygenation.

B. Ultrasonic Powering

Magnetic inductive powering is the most common and long-established method to energize implantable devices that cannot accommodate batteries [14]. If size is not a concern and the implant can accommodate a large-area coil (such as cochlear implants), this method is very attractive and is superior to other power transfer techniques. For miniature coils (mm and submm scale), however, coupling coefficient between the transmitter and receiver coils drops rapidly, making inductive powering inefficient and sensitive to angular misalignment. This is, in particular, serious in microdevices that need to be inserted through a needle, since such implants have to be narrow and long, hence, requiring a similar shape coil (either integrated or wirewound) with a very small flux capture cross section [15], [16].

Ultrasound is an alternative method to power implantable microdevices [17]–[19]. Although not as widespread as inductive powering, this technique provides several unique advantages including omnidirectionality and higher efficiencies at larger distances and smaller device sizes. The first advantage, i.e., omnidirectionality, is mainly due to the reflections of ultrasound at the body/air interfaces due to the large reflection coefficient at tissue air boundary. In situation where the ratio of the transducer size to the wavelength is much higher than the working distance, one is typically dealing with near-field ultrasound in which the original ultrasound beam is not really omnidirectional; however, wave reflections creates a homogenous medium [20]. Higher efficiencies in certain situations have been investigated theoretically by Denisov and Yeatman [21]. Their analysis shows that at small distances ($<$1 cm), inductive powering is more

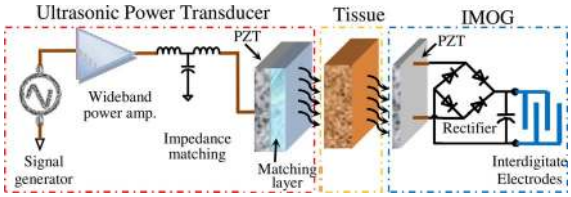

Fig. 2. Schematic of ultrasonic system used to power the IMOG.

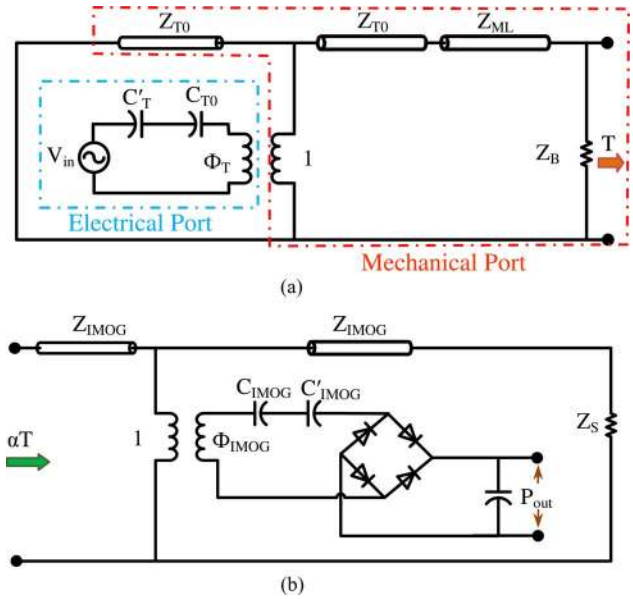

Fig. 3. KLM electromechanical model for (a) transmitter assuming air-baking on one side and matching layer ($Z_{\rm ML}$)/tissue Z_B on the other side, (b) receiver (i.e., IMOG).

efficient. However, between 1 and 10 cm of separations, the ultrasonic method is more efficient. In particular when receiver gets smaller than 2-mm ultrasound outperforms magnetic powering by three orders of magnitudes.

Fig. 2 shows a schematic of the ultrasonic system used to power the IMOG. The system can be divided into three parts: ultrasonic transmitter, tissue, and the IMOG. A signal generator produces the powering pulse sequence which is amplified by a wideband amplifier. The amplified signal is applied to the ultrasonic transmitter (lead zirconate titanate (PZT) in our case) through an impedance matching circuit. Matching is required since the output impedance of the amplifier is restive (50 Ω), while the ultrasonic transducer impedance is dominated by the imaginary part of the transducer electrode capacitance (∼80 nF in our transmitter). The ultrasonic power penetrates the tissue and excites the ultrasonic receiver of the IMOG (PZT in our case), generating an ac voltage. An embedded full-bridge rectifier converts this signal to a dc voltage that is then applied to the water in the interstitial fluid through a set of interdigitated electrodes.

The transmitter's Krimholtz, Leedom, Matthaei, (KLM) model correlating mechanical and electrical properties is depicted in Fig. 3(a). As for the mechanical properties, acoustic impedance of the transducer is modeled as a quarter wavelength transmission line on each side ($Z_{\rm T0}$); the matching layer acoustic impedance is also modeled as quarter wave length transmission line ($Z_{\rm ML}$), and the tissue load is modeled as the loss impedance (Z_B). The air-backed side acts like a short-circuited transmission line; hence, no power is transmitted on that side. Electrical properties are modeled with $C_{\rm T0}$ representing the transmitter parallel-plate capacitance due to the electrodes (∼80 nF), C'_T representing the frequency-dependent acoustic capacitance, and Φ_T representing the transformer ratio. The transmitter radiates mechanical power T into the tissue a fraction of which (αT, α is the attenuation of the ultrasonic power in tissue) is received and converted to the electrical power by IMOG.

Fig. 3(b) shows the electromechanical model of the receiver, i.e., IMOG, which is very similar to that of the transmitter. While in the transmitter, electrical port was the input and mechanical port was the output, in the IMOG (i.e., receiver), the acoustic/mechanical power (αT) is feeding the mechanical port while the generated electrical power is taken from the electrical port $P_{\rm out}$. Assuming the left side of the IMOG's receiver is toward the ultrasonic transducer, the ultrasonic power (αT) is impinged on this side and excites the representative mechanical port which has an acoustic impedance of $Z_{\rm IMOG}$. Part of the received mechanical power to the IMOG is reflected due to the acoustic mismatch between the tissue and the PZT, part of it is dissipated in the other mechanical port (attached to Z_S, acoustic impedance of the body), and the rest is converted to electrical power (1:$\Phi_{\rm IMOG}$ transformer ratio). Generated electrical power is then applied to the load (water in tissue) through $C_{\rm IMOG}$ (PZT parallel plate capacitance due to the electrodes ∼76 pF), C'_T (frequency-dependant acoustic capacitance), and the full-bridge rectifier.

Overall power transfer ratio (electrical input power at the transmitter to the electrical output power of the IMOG) can be written as

$$\frac{P_{\rm out}}{P_{\rm in}} = \Phi_T \times T_T \times \alpha \times \sigma \times \eta_{\rm IMOG} \times \eta_T \qquad (3)$$

where Φ_T and $\Phi_{\rm IMOG}$ are transformer ratios, $\alpha = e^{-2\mu x}$ is the attenuation (μ is the attenuation coefficient and x is the tissue depth through which ultrasound has traveled), σ is attenuation coefficient due to acoustic impedance mismatch between transducer and tissue, and η_T and $\eta_{\rm IMOG}$ are transducer and IMOG conversion ratios. Table I shows electromechanical properties of soft tissue and PSI-5A4E piezoceramic (Piezo Systems, Inc., MA) used as transducer/receiver materials in this study. By plugging these numbers into complex parameters of the KLM's equivalent circuit [22], one can calculate the power efficiency of the system to be around 0.1% [see (3)].

III. Fabrication Process

Fig. 4 illustrates the fabrication process flow for the IMOG. It started with a 300-μm-thick glass wafer. Glass was chosen over silicon to reduce parasitic capacitance and prevent unnecessary passivation layer deposition. Polymer substrates such as polyimide could also be used for further size reduction. Contact metallization (Ti/Pt, 400 Å/1000 Å) was performed using liftoff process [see Fig. 4(a)] followed by 100-nm plasma-enhanced

TABLE I
ELECTROMECHANICAL PROPERTIES OF THE TISSUE AND PZT

Property	Value	Unit
Transmitter/receiver density	7800	kg/m^3
Transmitter/receiver thickness	1.02	mm
Receiver area	5	mm^2
Transmitter area	52.4	cm^2
Piezoelectric Coefficient (d_{33})	390×10^{-12}	m/V
PZT Dielectric Constant	1800	N-A
PZT stiffness	1.47×10^{11}	N/m^2
Acoustic velocity in PZT	4355	m/s
Acoustic velocity in tissue	1540	m/s
Tissue density	950	Kg/m^3
Tissue attenuation coefficient	~0.54	dB/MHz/cm
Tissue thickness	3	cm

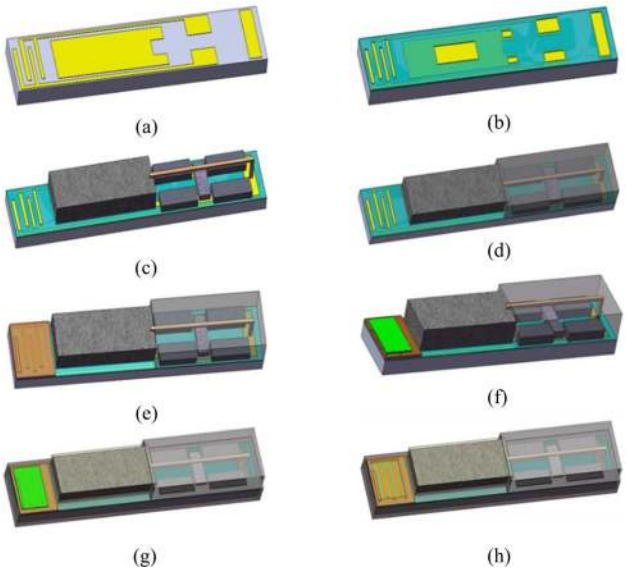

Fig. 4. IMOG fabrication process flow: (a) metalization, (b) exposed titanium passivation, (c) parts integration, (d) PDMS protection layer, (e) ion exchange membrane integration, (f) photoresist protection of ion exchange membrane, (g) parylene coating, and (h) parylene laser opening on the electrodes.

chemical vapor deposition nitride deposition and patterning [see Fig. 4(b)]. The nitride layer was required to protect the exposed adhesion promoter layer (titanium) at the side walls of the metalization. In the absence of the passivation layer, titanium would be etched electrochemically during IMOG operation, resulting in electrodes liftoff in less than 10 min [23], [24]. Next, discrete electronic parts including PZT (PSI-5A4E, Piezo Systems, Inc., MA), Schottky barrier diodes (NSR0130P2T5G, ON Semiconductor, CA), and 1-pF multilayer ceramic chip capacitor (C0603C0G1H010B, TDK, GA) were assembled on the substrate using silver epoxy (118-09A/B, creative materials) [see Fig. 4(c)]. The dimensions (1.02 mm $\times$ 1 mm $\times$ 5 mm) of the PZT bar was chosen to compromise between the size of the implant and body attenuation. Thinner PZT bar results in a higher resonance frequency and larger tissue attenuation [25]. Diodes, capacitors, and attachment wire were encapsulated by a polydimethylsiloxane (PDMS) droplet [see Fig. 4(d)]. A layer of 100-μm-thick CSO Selemion ion exchange membrane (AGC

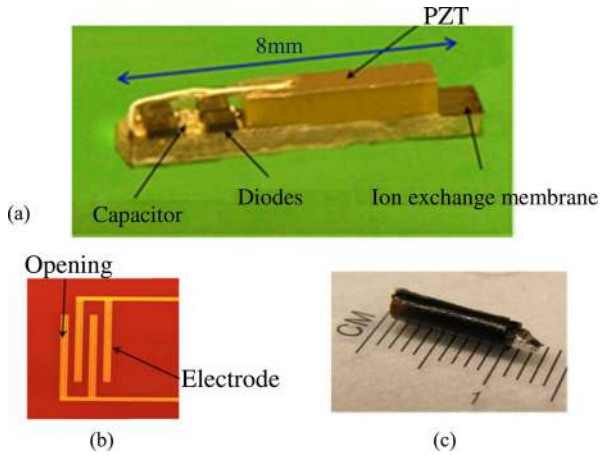

Fig. 5. Optical photograph of (a) fabricated IMOG, (b) interdigitated electrodes, and (c) IMOG encapsulated in an ion exchange membrane.

Engineering Co., Ibaraki, Japan) was attached on top of the electrodes using epoxy to block the chloride ions from reaching the electrodes [see Fig. 4(e)]. This membrane plays an important role in successful operation of IMOG.

Physiological saline (and all physiological fluids) contains dissolved sodium (Na^+) and chloride (Cl^-) ions. Performing water electrolysis without ion exchange membrane would produce oxygen and chlorine gases at the anode and hydrogen at the cathode. The anodic reactions are

$$2H_2O \rightarrow O_2 + 4H^+ + 4e^- \text{ and } 2Cl^- \rightarrow Cl_2 + 2e^-$$

while the primary cathodic reaction is

$$2H_2O + 2e^- \rightarrow H_2 + 2OH^-.$$

When Cl^- participates in the electrochemistry, the overall reaction is

$$2NaCl + 2H_2O \rightarrow Cl_2 + H_2 + 2NaOH.$$

This reaction, known as the chlor-alkali process, produces caustic soda (NaOH) and chlorine (Cl_2), both of which are harmful. To prevent chlor-alkali process, using ion exchange membrane is required.

For biocompatibility assurance, the whole device was encapsulated by 5-μm-thick chemical vapor deposition deposited parylene layer [see Fig. 4(g)]. Parylene coating was performed after covering the ion exchange membrane with photoresist [see Fig. 4(f)] to prevent parylene monomers from entering the ion exchange membrane and reducing its diffusivity. However, it should be mentioned that photoresist could not be backed as the maximum operation temperature of the ion exchange membrane is 65 °C. Finally, the parylene was removed at the electrodes location by laser micromachining and photoresist was dissolved in acetone [see Fig. 4(h)].

Fig. 5(a) shows an optical image of the fabricated IMOG composed of a PZT slab, a high-speed full-wave rectifier, and platinum electrodes covered by an ion exchange membrane. Interdigitated electrodes [see Fig. 5(b)] were used to create higher electric field with a fixed applied voltage resulting in an

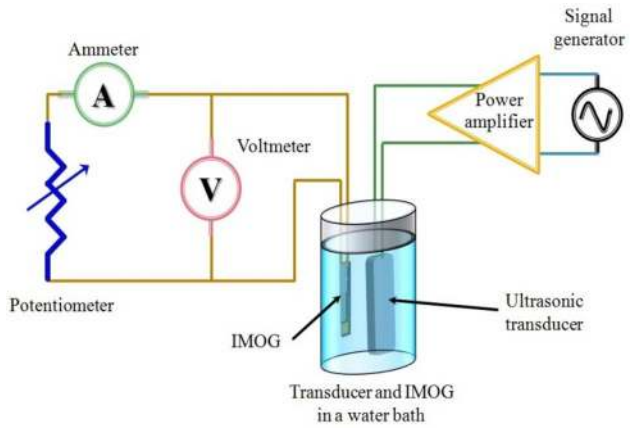

Fig. 6. Experimental setup to investigate the IMOG output characteristics.

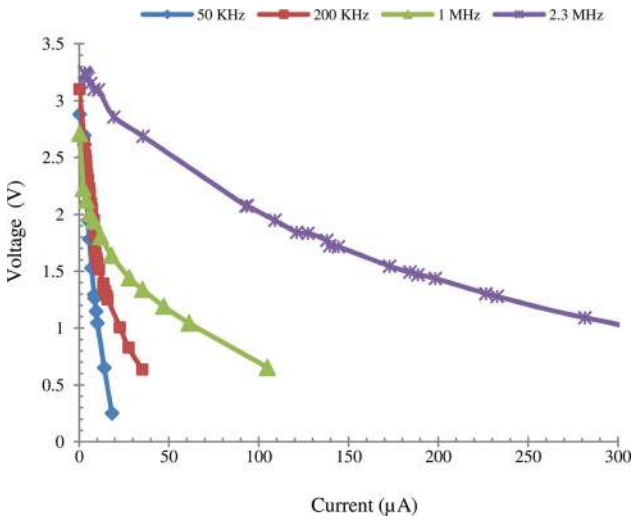

Fig. 7. IMOG's output characteristics at different frequencies.

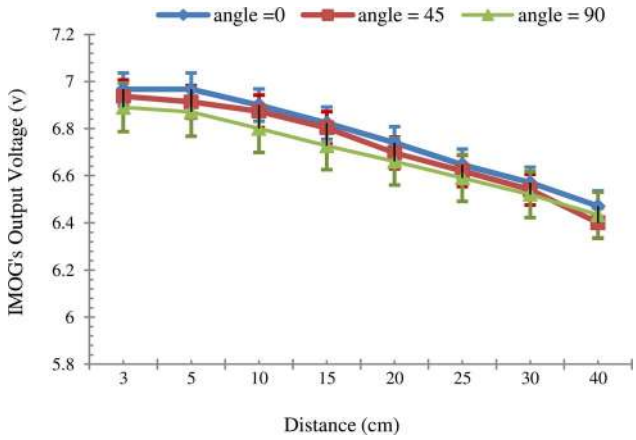

Fig. 8. IMOG output voltage versus distance between the IMOG and ultrasonic transducer at different angles.

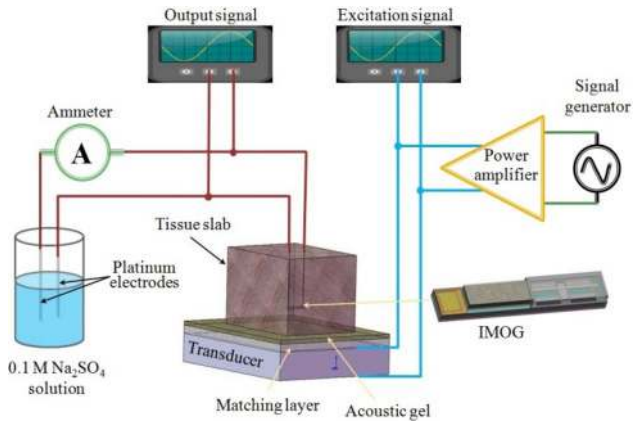

Fig. 9. Experimental setup for *in vitro* characterization of the IMOG operation. The IMOG generated voltage was applied into a 0.1 M sodium sulfate solution while monitoring the IMOG's output voltage and current.

enhanced electrolysis rate. Ion-exchange-membrane can also be used as a package to encapsulate the entire IMOG [see Fig. 5(c)].

IV. Experimental Results

A. In Vitro and Ex Vivo Characterizations

After fabricating the IMOG, the first experiment was conducted to investigate the IMOG *I–V* characteristics at different frequencies. The experimental setup is illustrated in Fig. 6. As depicted, IMOG and ultrasonic transmitter (1.02 mm × 72.4 mm × 72.4 mm) were immersed in DI water with the transmitter driven by a sinusoidal wave (50 $V_{p\text{-}p}$) using an ENI A300 power amplifier (Electronics & Innovation, Ltd., NY). Fig. 7 demonstrates the IMOG output characteristic at different frequencies. As expected, IMOG generated maximum output current at 2.3 MHz (resonance frequency of the PZT).

IMOG output voltage versus distance from the transmitter at different angles was also measured (see Fig. 8). As expected, the output voltage drops exponentially with distance. However, as can be seen, IMOG was capable of generating about 6.4 V even at separations of up to 40 cm. As mentioned earlier, another important characteristic of the IMOG is its minimal directionality which was verified in these experiments.

Fig. 9 shows the schematic of the *ex vivo* setup used to characterize the IMOG functionality. IMOG was inserted 3 cm deep into a pork muscle slab which included 1.5 cm of skin and subcutaneous fat. The tissue was placed on the top of the ultrasonic transmitter covered by an SU-8 acoustic impedance matching layer. Uncured PDMS was used as an acoustic gel. Transducer was excited by a 20% duty cycle square wave at 2.15 MHz. Due to the difficulty of in-tissue oxygen measurements, the output of the IMOG was applied to a 0.1 molar sodium sulfate solution outside the tissue. To minimize the electromagnetic coupling and noise due to the common ground, two separated oscilloscopes were used to monitor the transmitter excitation and IMOG output voltage.

An optical photograph of the setup is depicted in Fig. 10(a). Magnified pictures of the immersed platinum coated electrodes in the 0.1 molar sodium sulfate is shown in Fig. 10(b). Oxygen bubbles were observed 5 min after turning on the ultrasonic transducer. Output currents as high as 300 μA were recorded, exceeding the 20 μA *in vivo* requirement.

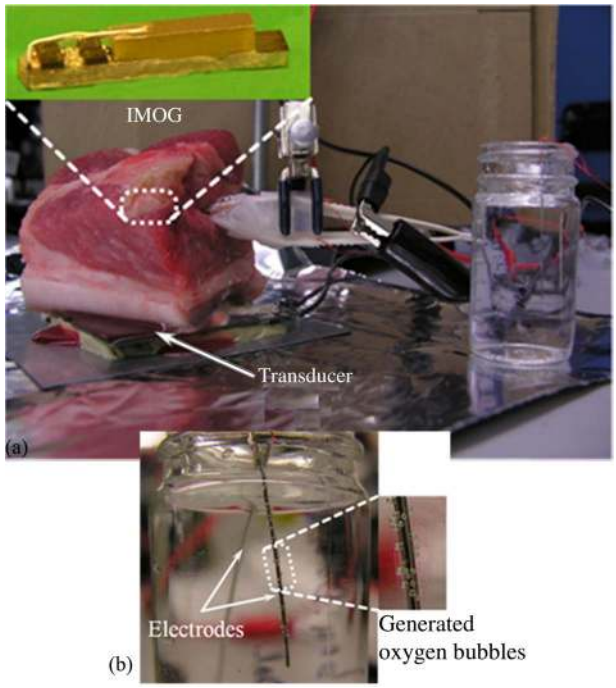

Fig. 10. (a) Optical photograph of the experimental setup used for *ex vivo* characterizations: IMOG is inserted in a slab of tissue, and the output is applied to $Na_2 So_4$ solution. (b) Oxygen bubbles were generated by IMOG in the solution.

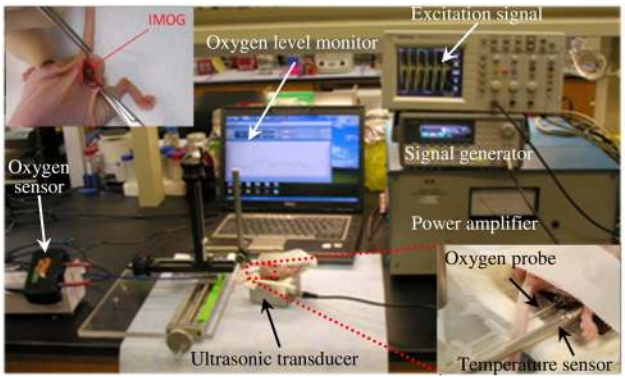

Fig. 11. Experimental setup for real-time *in vivo* oxygen measurements during tumor oxygenation by IMOG. Tumor oxygen levels and temperature were monitored by NeoFax measurement system, while the transmitter power was monitored by an oscilloscope.

B. In Vivo Characterizations

After successful *in vitro* characterizations, two experiments were designed to study the *in vivo* operation of the IMOG. These included real-time monitoring with an oxygen probe and optical imaging with luciferase assay. Fig. 11 illustrates the experimental setup for *in vivo* real-time oxygen monitoring. The IMOG was implanted in a BxPC-3 pancreatic tumor model grown in the flanks of the athymic mice (see top left inset in Fig. 11). The tumors size was small (≈10 mm × 8 mm × 5 mm); hence only the electrode portion of the IMOG resided within the tumor (the rest of IMOG was placed under the skin). This experiment was conducted on three mice; each had two tumors.

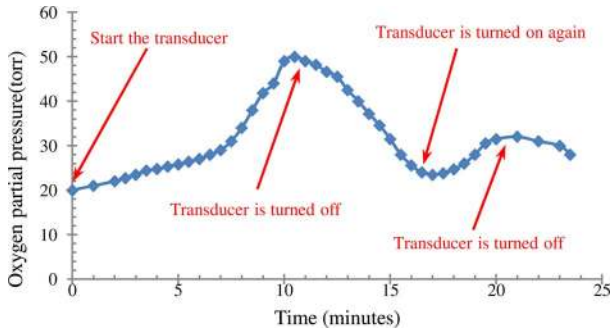

Fig. 12. *In vivo* tumor oxygenation showing IMOG's capability in elevating oxygen levels in a hypoxic tumor in less than 10 min.

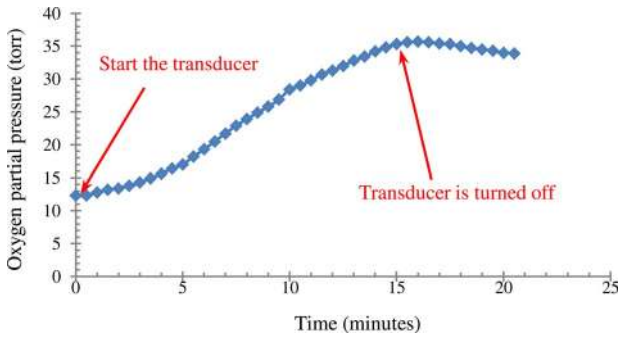

Fig. 13. *In vivo* tumor oxygenation using IMOG two weeks after implantation.

One of the tumors was used as control, i.e., with no IMOG implantation, while the other one was oxygenated by IMOG.

A day after IMOG implantation, the mouse was immobilized on the ultrasonic transmitter, a hole was created in the tumor by small needle, and an oxygen probe (21G, Ocean Optics Inc., FL) was inserted into the tumor (see bottom right inset in Fig. 11). NeoFox measurement system (Ocean Optics Inc., FL) which is a fluorescence-based optical sensor detects both dissolved oxygen and operating temperature.

Two mice out of the three survived during the experiments. Oxygen level in a tumor with IMOG in one of these mice is plotted in Fig. 12. As can be seen, IMOG is capable of oxygenating the tumors in less than 10 min. The experiment had to be stopped after a short time due to the loss of anesthesia in mice. We did not notice any oxygen change in the tumors without the IMOG.

To study the biofouling and other physiological effects on the IMOG's operation, we conducted the aforementioned experiment again two weeks after IMOG implantation (see Fig. 13). As illustrated, IMOG was operational even two weeks after implantation. The mice expired after these experiments and we could not perform measurements for a longer period.

To further validate the IMOG's operation, we conducted an *in vivo* bioluminescence study. Due to its immediate availability, CWR-22rv prostate tumors containing constitutively expressing firefly luciferase gene expression cassette was used to qualitatively monitor artificially generated oxygen. In luminescent reactions, the oxidation of luciferin will produce light at around 560 nm. The rates of the reaction between luciferin and oxygen

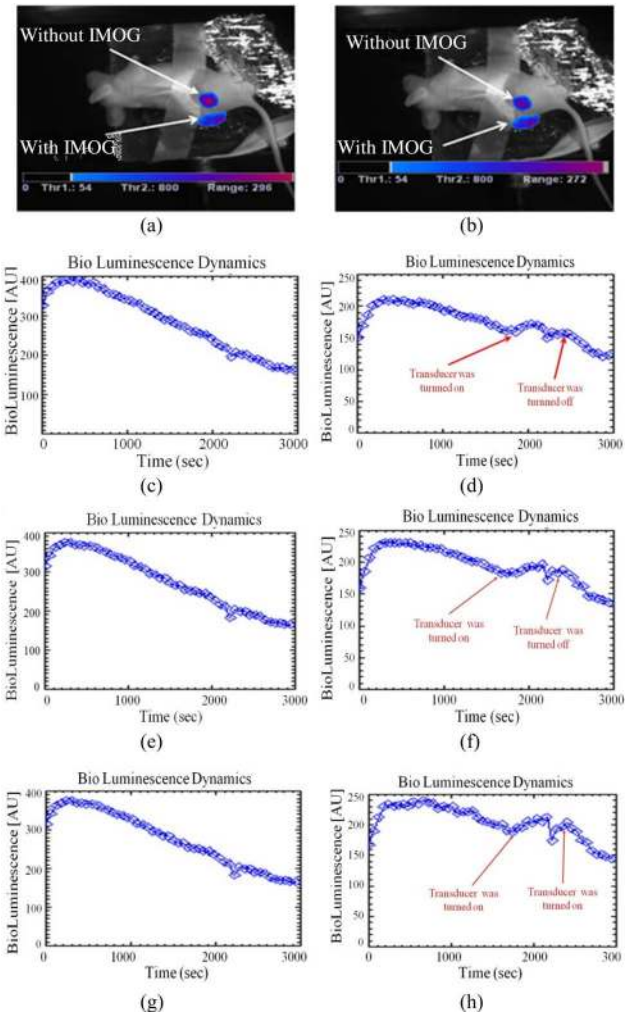

Fig. 14: *In vivo* luciferase study: (a), (b) color images of a tumor 1 min before and 6 min after IMOG operation. (c)–(h) Bioluminescence dynamic diagrams of tumors without (left hand) and with the IMOG (right hand).

are extremely slow unless they are catalyzed by luciferase in the presence of adenosine-5′-triphosphate (ATP) [26]:

$$\text{luciferin} + \text{ATP} \rightarrow \text{luciferyl adenylate} + \text{Pyrophosphates (PPi)}$$

$$\text{luciferyl adenylate} + \text{O}_2 \rightarrow \text{oxyluciferin} + \text{Adenosine monophosphate (AMP)} + \text{light}$$

Similar to the previous study, two similar tumors were grown in the flanks of the athymic mice. Assuming the saturation of ATP and luciferin in the two tumors, oxygen concentration will be the key factor determining the output of bioluminescence signal. The IMOG was implanted only in one of the two tumors and experiments were performed on three mice. The bioluminescence assay study was performed one day after IMOG implantation. Before and after intraperitoneal injection of D-Luciferin (Xenogen, Alameda, CA) with a concentration of 150 mg/kg body weight, sequential images were taken by Night-OWL optical imager (Berthold Technologies**,** Germany) at an exposure rate of 30 s and a sample rate of 1 min. IMOG was turned on for 10 min and then turned off during the imaging process.

Fig. 14(a) and (b) shows the colored images of the tumors 1 min before turning on the transducer and 6 min after transducer operation. As can be seen, brightness (red) reduction in the tumor with IMOG is much less than that of the tumor without IMOG. Fig. 14(c)–(h) represents the bioluminescence dynamic diagrams of the tumors in three different pixels. The left- and right-hand side plots represent the tumors without and with IMOG, respectively, for each pixel. As illustrated, bioluminescence intensity in tumors that have no IMOG decayed continuously after a first peak, while a second peak is observable for the tumors that have an IMOG. The presence of this second peak in the bioluminescence plot of all the tumors with IMOG clearly proves that oxygen is generated by the IMOG.

V. Conclusion

In conclusion, we presented an implantable microdevice for *in situ* tumor oxygenation. Our device uses ultrasonic powering which has less directionality and provides greater power transmission efficiencies at larger separations and smaller receiver dimensions. The small size of the device (1.2 mm × 1.3 mm × 8 mm) makes it potentially suitable for direct intratumor insertion using a biopsy needle. *In vitro, ex vivo,* and *in vivo* characterizations of the microimplant were presented, verifying its functionality in clinically relevant settings.

Acknowledgment

The authors would like to thank the technical staff at the Purdue University Birck Nanotechnology Center for their assistance in microfabrication.

References

[1] P. Rubin and J. P. Williams, Eds., *Clinical Oncology: A Multi-Disciplinary Approach for Physicians & Students*. Philadelphia, PA: Saunders, 2001.
[2] E. C. Halperin, C. A. Perez, L. W. Brady, D. E. Wazer, C. Freeman, and L. R. Prosnitz, Eds., *Perez and Brady's Principles and Practice of Radiation Oncology.*. Baltimore, MD: Williams & Wilkins, 2007.
[3] J. S. Tobias, "Clinical Practice of Radiotherapy," *The Lancet*, vol. 339, no. 8786, pp. 159–163, 1992.
[4] E. J. Hall and A. J. Giacca, *Radiobiology for Radiologist*. Baltimore, MD: Williams & Wilkins, 2005.
[5] W. F. Morgan and M. B. Sowa, "Effects of ionizing radiation in nonirradiated cells," *Proc. Natl. Acad. Sci.*, vol. 102, no. 40, pp. 14127–14128, 2005.
[6] P. Vaupel, F. Rallino, and P. Okunieff, "Blood flow, oxygen and nutrient supply and metabolic microenvironment of human tumors: A review," *Cancer Res.*, vol. 49, pp. 6449–6465, 1989.
[7] P. Vaupel, "Pathophysiology of Solid Tumors," in *The Impact of Tumor Biology on Cancer Treatment and Multidisciplinary Strategies*. Berlin, Germany: Springer-Verlag, 2009, pp. 51–92.
[8] J. M. Brown and A. J. Giaccia, "The unique physiology of solid tumors: Opportunities (and problems) for cancer therapy," *Cancer Res.*, vol. 58, pp. 1408–1416, 1998.
[9] S. E. Partridge, C. Aquino-Parsons, C. Luo, A. Green, and P. L. Olive, "A pilot study comparing intratumoural oxygenation using the comet assay following 2.5% and 5% Carbogen and 100% Oxygen," *Int. J. Radiat. Oncol. Biol. Phys.*, vol. 49, no. 2, pp. 575–580, 2001.
[10] M. R. Horsman and J. Overgaard, "Preclinical studies on how to deal with patient intolerance to nicotinamide and carbogen," *J. Radiother. Oncol.*, vol. 70, no. 3, pp. 301–309, 2004.
[11] J. Daruwalla and C. Christophi, "Hyperbaric oxygen therapy for malignancy: A review," *World J. Surgery*, vol. 30, no. 12, pp. 2112–2131, 2006.

[12] H. Wu, E. S. Avgoustiniatos, L. Swette, S. Bonner-Wei, G. C. Weir, and C. K. Colton, "In situ electrochemical oxygen generation with an immunoisolation device," *Ann. New York Acad. Sci.*, vol. 875, pp. 105–125, 1999.
[13] D. Tromans, "Modeling oxygen solubility in water and electrolyte solutions," *Ind. Eng. Chem. Res.*, vol. 39, pp. 805–812, 2000.
[14] K. van Schuylenbergh and R. Puers, *Inductive Powering: Basic Theory and Application to Biomedical Systems*. New York: Springer-Verlag, 2009.
[15] P. R. Troyk, "Injectable electronics," *Annu. Rev. Biomed. Eng.*, vol. 1, pp. 177–209, 1999.
[16] B. Ziaie, M. D. Nardin, A. R. Coghlan, and K. Najafi, "A single channel implantable microstimulator for functional neuromuscular stimulation," *IEEE Trans. Biomed. Eng.*, vol. 44, no. 10, pp. 909–920, Oct. 1997.
[17] S. Arra, J. Leskinen, J. Heikkila, and J. Vanhala, "Ultrasonic power and data link for wireless implantable applications," in *Proc. IEEE Int. Symp. Wireless Pervasive Comput.*, San Juan, Puerto Rico, 2007, pp. 567–571.
[18] H. Kawanabe, T. Katane, H. Saotome, O. Saito, and K. Kobayashi, "Power and interactive information transmission to implanted medical device using ultrasonic," *Japn. J. Appl. Phys.*, vol. 41, no. 1#5B, pp. 3600–3603, 2002.
[19] Y. Rozenman, R. S. Scwartz, H. Shah, and K. H. Parikh, "Wireless acoustic communication with a miniature pressure sensor in the pulmonary artery for disease surveillance and therapy of patients with congestive heart failure," *J. Am. College Cardiol.*, vol. 49, pp. 784–789, 2007.
[20] K. K Shung and M. Zippuro, "Ultrasonic transducers and arrays," *IEEE Eng. Med. Biol.*, vol. 15, no. 6, pp. 20–30, Nov./Dec. 1996.
[21] A. Denisov and E. Yeatman, "Ultrasonic vs. inductive power delivery for miniature biomedical implants," in *Proc. Int. Conf. Body Sensor Networks*, Singapore, 2010, pp. 84–89.
[22] G. S. Kino, *Acoustic Waves: Design Imaging and Analog Signal Processing*. Englewood Cliffs, NJ: Prentice-Hall, 1987.
[23] M. A. Khan, R. L. Williams, and D. F. Williams, "In-vitro corrosion and wear of titanium alloys in the biological environment," *Biomaterials*, vol. 17, pp. 2117–2126, 1996.
[24] J. E. G. Gonzalez and J. C. Mirza-Rosca, "Study of the corrosion behavior of titanium and some of its alloys for biomedical and dental implant applications," *J. Electroanalytical Chem.*, vol. 471, pp. 109–115, 1999.
[25] K. K. Shung and G. A. Thieme, *Ultrasonic Scattering in Biological Tissues*. Boca Raton, FL: CRC Press, 1992.
[26] S. J. Gould and S. Subramani, "Firefly luciferase as a tool in molecular and cell biology," *Anal. Biochem.*, vol. 175, no. 1, pp. 5–13, 1988.

Teimour Maleki (M'09) received the B.Sc. degree in biomedical engineering from Amirkabir University of Technology, Tehran, Iran, in 2000, the M.Sc. degree in electrical engineering from University of Tehran, Tehran, in 2003, and the Ph.D degree in electrical engineering from Purdue University, West Lafayette, IN, in 2010.

He is currently a Research Assistance Professor at Birck Nanotechnology Center, Purdue University. His research interests include developing micro/nanodevices and implantable microsystems for healthcare.

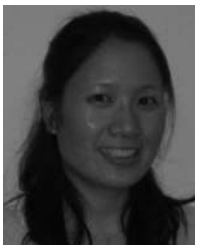

Ning Cao received the B.S. degree in biological sciences from Fudan University, Shanghai, China, in 2004. She is currently working toward the Ph.D. degree majoring in medical physics at School of Health Sciences, Purdue University, West Lafayette, IN.

Her research interests include utilization of *in vivo* imaging modalities to develop methods sensitizing pancreatic cancer to radiotherapy through tumor reoxygenation.

Seung Hyun Song received the B.S. degree in electrical engineering from the Iowa State University, Ames, in 2009. He is currently working toward the Ph.D degree in electrical and computer engineering at Purdue University, West Lafayette, IN.

His current research interests include implantable microdevices utilizing various powering schemes for biomedical applications.

Chinghai Kao, photograph and biography not available not available at the time of publication.

Song-Chu "Arthur" Ko received the M.D. degree from the University of Texas Medical School, Houston, in 1992, and the Ph.D. degree from MD Anderson Cancer Center, University of Texas Graduate School of Biomedical Sciences, Houston, 1998. He did his residency in radiation oncology in the College of Physicians and Surgeons, Columbia University, New York, in 2006.

He was a Postdoctoral Fellow in radiation biology in the Columbia University Center for Radiological Research, New York. He is currently an Assistant Professor of clinical radiation oncology at Indiana University School of Medicine, Indianapolis. His research interests include genitourinary malignancies and research, proton/particle beam therapy, and brachytherapy.

Babak Ziaie (A'95–M'00–SM'07) received the Ph.D. degree in electrical engineering from the University of Michigan, Ann Arbor, in 1994.

From 1995 to 1999, he was a Postdoctoral Fellow and an Assistant Research Scientist at the Center for Integrated Microsystems, University of Michigan. He was subsequently (1999–2004) with the Electrical and Computer Engineering Department, University of Minnesota, Twin Cities, as an Assistant Professor. Since January 2005, he has been with the School of Electrical and Computer Engineering, Purdue University, West Lafayette, IN, where he is currently a Full Professor. His research interests include biomedical applications of micro- and nanoelectromechanical systems.